PROCEEDINGS OF SPIE

UAV-based multi-sensor multi-platform integration for high throughput phenotyping

Radhika Ravi, Seyyed Meghdad Hasheminasab, Tian Zhou, Ali Masjedi, Karoll Quijano, et al.

SPIE.

UAV-based Multi-sensor Multi-platform Integration for High Throughput Phenotyping

Radhika Ravi, Seyyed Meghdad Hasheminasab, Tian Zhou, Ali Masjedi, Karoll Quijano, John Evan Flatt, Melba Crawford, Ayman Habib
Lyles School of Civil Engineering, Purdue University, West Lafayette, IN USA 47907

ABSTRACT

In recent days, phenotyping of various crops is gaining widespread popularity due to its ability to recognize variations in the effects of different genotypes of a particular crop in terms of its growth, yield, biomass, and so on. Such an application requires extensive data collection and analysis with a high spatial and temporal resolution, which can be attained using multiple sensors onboard Unmanned Aerial Vehicles (UAVs). In this study, we focus on harnessing information from a variety of sensors, such as RGB cameras, LiDAR units, and push-broom hyperspectral sensors – Short-wave Infrared (SWIR) and Visible Near Infrared (VNIR). The major challenge that needs to be overcome in this regard is to ensure an accurate integration of information captured across several days from the different sensor modalities. Moreover, the payload constraint for UAVs restrain us from mounting all the sensors simultaneously during a single flight mission, thus entailing the need for data capture from different sensors mounted on separate platforms that are flown individually over the agricultural field of interest.

The first step towards integration of different data modalities is the generation of georeferenced products from each of the flight missions, which is accomplished with the help of Global Navigation Satellite Systems (GNSS) and Inertial Navigation Systems (INS) mounted on the UAVs that are time-synchronized with the onboard LiDAR units, cameras and/or hyperspectral sensors. Furthermore, an accurate georeferencing is achieved by developing robust calibration approaches dedicated towards accurate estimation of mounting parameters of the involved sensors. Finally, the geometric and spectral characteristics, such as canopy cover and leaf count, derived from the different sensors are used to devise a model to analyze the phenotypic traits of crops. The preliminary results indicate that the proposed calibration techniques can attain an accuracy of upto 3 cm.

Keywords: High-throughput phenotyping, UAV, LiDAR units, RGB cameras, hyperspectral sensors, system integration and calibration, accurate georeferencing, GNSS/INS

INTRODUCTION

Precision agriculture involves better management of farm inputs such as fertilizers, herbicides, seed, fuel (used during tillage, planting, spraying, etc.) by doing the right management practice at the right place and the right time. According to a recent study by Tilman et al. [1], an increase of 100-110% is forecast in global crop demand by 2050 as compared to 2005. In order to meet this demand with minimal environmental impacts, attainment of high yields on existing croplands is of great importance. Phillips [2] stated genetic improvement of staples has accounted for more than half of the past increases in yields. Recent advances in technology provide the ability to use various remote sensing techniques for precision agriculture applications. High throughput phenotyping is one of such advances that is gaining wide recognition as it has proven to be an efficient method to non-destructively capture plant traits. Araus & Cairns [3] conducted a detailed study on the advancement of field high throughput phenotyping that is required for increasing the efficiency of crop genetic improvement to meet the needs of future generations. They concluded that the capacity for undertaking precision phenotyping, particularly under repeatable and representative growing conditions in the field, is lagging far behind the capacity to generate genomic information, thus constraining breeding advances. So, it is imperative to develop data collection platforms that facilitate repetitive data acquisitions with high spatial resolution over agricultural fields in order to extract accurate phenotypic traits for plants corresponding to different breeding techniques. In recent years, UAV-based platforms have been proving to be low-cost platforms that can carry a multitude of sensors to provide a wide spectrum of data if flown over agricultural fields. Moreover, their relatively easy deployment enables repetitive data acquisitions, thus

facilitating an analysis of the temporal variation of crop traits with minimal human intervention. In this paper, we explore the data acquired by three different sensors – RGB cameras, LiDAR sensors, and hyperspectral sensors. Passive sensors, including RGB cameras, push-broom hyperspectral (Visible Near Infrared – VNIR and Short Wave Infrared – SWIR) sensors, can provide rich spectral/color information as well as positional information of objects of interest. For images captured by passive sensors, accurate 3D information can be derived through an image-based 3D reconstruction procedure. Active sensors, such as LiDAR systems, are able to directly provide precise and reliable 3D information for the scanned area. Moreover, due to recent improvements in the accuracy of integrated Global Navigation Satellite Systems (GNSS) and Inertial Navigation Systems (INS), the data captured by both passive and active sensors mounted on UAV can be georeferenced with high spatial accuracy. However, in order to exploit the full extent of data provided by these sensors, it is essential to first develop robust calibration techniques for each of these sensors in order to accurately integrate the data from the different modalities captured over a period of time. In this paper, we propose strategies for the calibration of a UAV platform carrying these sensors to estimate the mounting parameters, i.e., the lever-arm and boresight parameters, relating each of the sensors to the onboard GNSS/INS unit. Finally, we use the data acquired from the calibrated system to derive geometric and spectral characteristics from the different sensors to devise a model to analyze the phenotypic traits of crops.

Over the past few years, extensive research has been conducted for the calibration of airborne mobile mapping systems consisting of laser scanners [4], [5], [6], [7]. Similarly, several techniques have been developed to accurately calibrate different types of cameras in order to obtain accurate estimates of their intrinsic and extrinsic parameters [8], [9], [10]. Although many procedures have been developed for LiDAR system calibration and camera calibration separately, the simultaneous calibration of a mapping system consisting of both LiDAR units and cameras is an area of research that is still under exploration. Castorena et al. [11] devised a method for automatic extrinsic calibration and sensor fusion for a system comprised of a LiDAR and an optical camera by exploiting the natural alignment of depth and intensity edges. However, this approach demands the availability of depth maps and intensity images for accurate calibration and cannot be applied in case of an inavailability of either of these information. Levinson & Thrun [12] devised an approach for real-time miscalibration detection and correction by using a probabilistic background monitoring algorithm. Although their approach can accurately detect small incremental values to attain accurate calibration, they have not addressed the issue of accurate calibration starting with significantly inaccurate initial estimates for the parameters. However, this problem is mitigated by the calibration approach proposed in this paper for an integrated LiDAR and camera system based on the use of conjugate points and linear/planar features in overlapping images and point clouds derived from different flight lines.

For push-broom scanners, significant research has been dedicated towards establishing reliable boresight calibration strategies. Muller et al. [13] proposed a boresight calibration approach for airborne and space borne push-broom scanners. Here, using the interior orientation parameters, GNSS/INS georeferencing parameters, nominal lever arm components and boresight angles, and an available Digital Elevation Model (DEM), the image points corresponding to established GCPs were projected onto the DEM and boresight angles were estimated by minimizing the differences between the GCPs and the projected ground coordinates. Based on the conceptual basis of the approach proposed in [13], similar strategies involving additional parameters (e.g., aircraft stabilizer scaling factors and variations of sensor's CCD size) in the calibration procedure were discussed in [14] and [15]. The key limitation of the above approaches is the need for having a DEM of the covered area as well as some GCPs. In this paper, the hyperspectral push-broom scanner system is calibrated by a rigorous approach using tie features by enforcing an optimal intersection of the light rays connecting the perspective centers of the imaging scanner, object point, and the respective image points.

An experimental setup is used to evaluate the performance of the proposed calibration procedure for UAV-based integrated LiDAR and camera system through the a-posteriori variance factor of the Least Squares Adjustment (LSA) procedure and the quality of fit of the adjusted LiDAR point cloud and image points to linear/planar surfaces before and after the calibration process. The accuracy of the boresight calibration strategy for hyperspectral push-broom scanners is evaluated by using the estimated boresight angles for ortho-rectification of six hyperspectral UAV datasets acquired over an agricultural field. Qualitative and quantitative evaluations of the results have shown significant improvement in the derived orthophotos to a level equivalent to the Ground Sampling Distance (GSD) of the used scanner. Finally, the calibrated system is used to derive accurately georeferenced data from the different sensors and use it to extract plant characteristics, such as height percentile, canopy volume, canopy cover, height histogram, and hyperspectral vegetation indices. These features are further used in Support Vector Regression models to predict the biomass of different genotypes of the same crop.

UAV SYSTEM INTEGRATION

The UAV-based system used in this study was developed using a DJI M600 as the platform to mount the LiDAR units, RGB cameras, and hyperspectral sensors. Figure 1 shows an integrated UAV platform along with the mounted sensors. This UAV-based system consists of a Velodyne Puck LITE LiDAR unit, a Sony Alpha 7R-III RGB camera with 28mm Sony lens, and a Headwall Nano-Hyperspec push-broom scanner along with an Applanix APX-15v3 GNSS/INS unit for direct georeferencing. The Velodyne Puck Lite LiDAR unit has a typical range accuracy of 3 cm. The Sony Alpha 7R-III camera is a 42.2 MP full-frame mirrorless camera. This selection supports the goal of having maximum image resolution to facilitate accurate orthophoto generation and 3D point cloud reconstruction. The Headwall Nano-Hyperspec covers 270 spectral bands ranging between 400 nm and 1000 nm with a band width of 2.2 nm. Each scan line contains 640 pixels with a pixel pitch of 7.4 µm. The focal length of the lens used on the Nano-Hyperspec push-broom scanner is 8.2 mm, which corresponds to roughly 3.5 cm GSD when flying at 40 m above ground. For the APX-15 unit, the post-processed positional accuracy is 2 to 5 cm and the predicted accuracy for the roll/pitch and heading is 0.025 and 0.08˚, respectively.
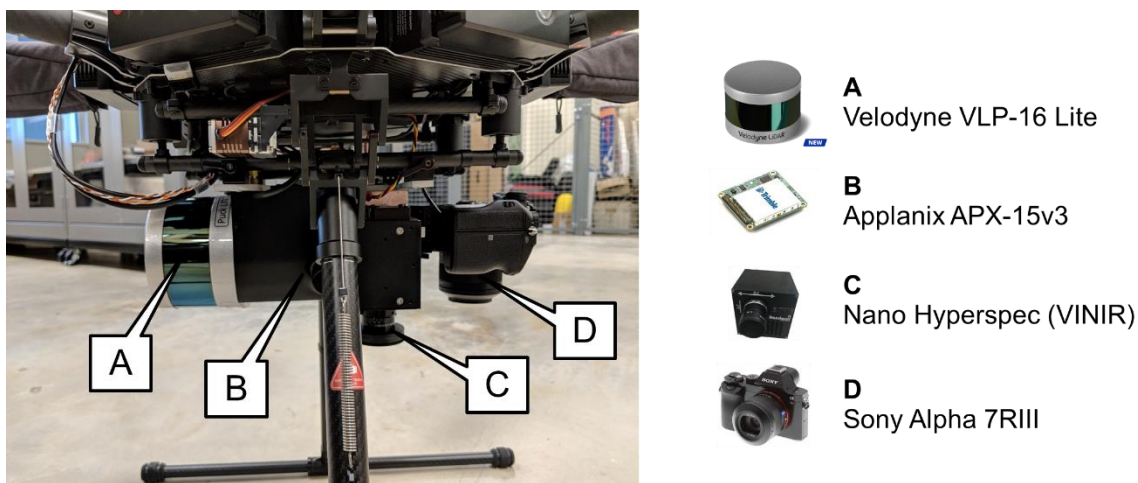

Figure 1. UAV-based multi-sensor system consisting of LiDAR unit, RGB camera, hyperspectral push-broom scanner, and GNSS/INS unit.

MATHEMATICAL MODELS FOR DIFFERENT SENSORS

In this paper, we propose calibration strategies to estimate the mounting parameters relating the different sensors (LiDAR, RGB camera, and hyperspectral scanner) to the onboard GNSS/INS unit in order to derive accurately georeferenced data from them. However, in order to proceed to developing a calibration strategy, we start here by briefly stating the mathematical models associated with each of these sensors and state the objectives of system calibration, i.e., the unknown parameters that require to be accurately estimated.

RGB Frame Camera

A typical GNSS/INS-assisted frame camera system would involve 3 coordinate systems (i.e., mapping frame, IMU body frame, and camera coordinate frame). A given point, I, captured in an image as point, i, from a camera onboard a mobile mapping system can be reconstructed in the mapping coordinate system using Equation 1. Here, $r_i^C(t)$ denotes the distortion-free coordinates of a point, i, in an image captured by camera, C, relative to the camera coordinate system. The camera (C) is related to the IMU body frame by a rigidly defined lever arm, r_C^b, and boresight matrix, R_C^b. Finally, each point, i, in an image captured by camera, C, at time, t, has a scaling factor associated with it, which is denoted by $\lambda(i, C, t)$. The GNSS/INS integration provides the time dependent position, $r_b^m(t)$, and rotation, $R_b^m(t)$, relating the mapping frame and IMU body frame coordinate systems, according to the optimized solution from the available GNSS and inertial measurements. The unknowns that need to be calibrated in case of a frame camera include the lever arm, r_C^b, the boresight angles constituting R_C^b, and the scaling factors, $\lambda(i, C, t)$ for all the image points used for calibration.

$$r_I^m = r_b^m(t) + R_b^m(t)\, r_C^b + \lambda(i, C, t)\, R_b^m(t)\, R_C^b\, r_i^C(t) \tag{1}$$

LiDAR Unit

A typical LiDAR system would involve 3 coordinate systems (i.e., mapping frame, IMU body frame, and laser unit frame). A given point, I, acquired from a mobile mapping system equipped with a laser scanner can be reconstructed in the mapping coordinate system using Equation 2. Here, $r_I^{lu}(t)$ denotes the coordinates of a 3D point relative to the laser unit coordinate system. The laser unit (lu) is related to the IMU body frame by a rigidly defined lever arm, r_{lu}^b, and boresight matrix, R_{lu}^b. Here, the unknowns to be estimated during calibration are the lever arm, r_{lu}^b, and the boresight angles constituting the matrix, R_{lu}^b.

$$r_I^m = r_b^m(t) + R_b^m(t) \, r_{lu}^b + R_b^m(t) \, R_{lu}^b \, r_I^{lu}(t) \tag{2}$$

Hyperspectral Push-broom Scanner

The calibration approach used for a hyperspectral push-broom scanner is based on a collinearity equation model, where the image coordinates are represented as a function of the GNSS/INS position and orientation, ground coordinates of the tie features, lever arm components, and the boresight angles, as represented by Equation 3. Here, the lever arm is assumed to be measured accurately, while the boresight angles need to be estimated. To eliminate the unknown scale factor λ_i from Equation 3, the first and second rows can be divided by the third one, thus resulting in two equations involving the unknown boresight angles $(\Delta\omega, \Delta\varphi, \Delta\kappa)$ and the ground coordinates of the tie features, r_I^m.

$$r_i^c = {}^1\!/_{\lambda_i} \, R_b^c \, \{ R_m^b(t) \, [r_I^m - r_b^m(t)] - r_c^b \} \tag{3}$$

METHODOLOGY

Simultaneous LiDAR-Camera Calibration

An integrated LiDAR and camera system calibration aims to simultaneously estimate all the system parameters so as to minimize the discrepancies among conjugate points, linear features, and/or planar features obtained from different laser scanners, cameras, and/or flight lines. In this research, we developed a point-pairing-based technique for bundle adjustment of images as well as the integration of LiDAR and image points in order to conduct a simultaneous calibration of the two sensors. This is achieved by imposing an equality constraint on the 3D mapping frame coordinates computed for different LiDAR/image points representing the same object point by pairing them together. However, owing to the irregular distribution of LiDAR points leading to inaccurate point-to-point correspondence, this research proposes an incorporation of linear/planar features which are represented in LiDAR scans/images as a sequence of pseudo-conjugate points lying along the features. The equality constraint is then updated using a modified weight matrix for each feature to ensure the elimination of non-random discrepancy along the feature to which a point pair belongs. In other words, a modified weight matrix for a planar feature would retain the component of discrepancy only along the direction normal to the plane. Similarly, in case of a linear feature, the discrepancy along the direction of the line is nullified for any point pair belonging to the feature. A detailed analysis on the contribution of pairings for different types of features (points, lines, and planes) is conducted to develop an optimal pairing strategy between LiDAR scans and images [16]. As a result, the following pairing scheme is designated to be optimal in order to conduct an integrated LiDAR and camera system calibration:

- Image-to-image conjugate point pairing,

- LiDAR-to-LiDAR and LiDAR-to-image pairings of pseudo-conjugate points belonging to corresponding linear features,

- LiDAR-to-LiDAR pairings of pseudo-conjugate points along corresponding planar features, and

- LiDAR-to-image pairings of pseudo-conjugate points belonging to corresponding planar features (which have distinct points that can be identified in images) along with image-to-image conjugate point pairs for the same feature.

This research carries out an iterative calibration procedure where the discrepancy among extracted points/features is minimized using a modified weight matrix to derive mounting parameters through a Least Squares Adjustment (LSA) process.

Hyperspectral Push-broom Scanner Calibration

The proposed calibration approach for a hyperspectral push-broom scanner is based on using identified tie features in the push-broom scanner scenes to estimate the boresight angles. The boresight angles are estimated by enforcing the

coplanarity constraint relating conjugate features in overlapping push-broom hyperspectral scenes. In this case, since one is dealing with a non-linear model in the involved unknowns, as given in Equation 3, an iterative LSA procedure is used starting from approximate values of the unknowns. A tie point that is observed in n scenes will lead to 2n equations in 6 unknowns. The optimal/minimal configurations of the flight line and tie point distribution derived by Habib & Zhou [17] is used to derive a reliable estimate of the boresight angles and ground coordinates of tie points.

Biomass Prediction using Geometric and Spectral Characteristics of Crops

In this study, the accurately georeferenced 3D point cloud obtained from the onboard LiDAR unit is used to extract valuable characteristics of crops representing different genotypes of the same plant. The traits of interest include the following:

- Height percentile: From the LiDAR-based 3D point cloud acquired over different dates for the different crops, the 30th, 50th, 75th, 90th, 95th, 99th, and 100th percentile height values were extracted for each plot that represents a particular genotype of the crop. This facilitates the monitoring and comparison of the rate of growth of plants with different genotypes.
- Canopy Volume: To estimate some phenotypic traits, such as biomass, it is beneficial to estimate some volume-related characteristics of the canopy from LiDAR data. This is done by assigning grids with user-defined cell dimensions to each plot and then, calculating the height of each cell from the points located in that cell by taking the average of the heights of the lowest point and the highest point. This height multiplied by the size of the cell is considered to be the estimate of the volume of canopy of each cell, and then the sum of the volume of all the cells in each plot was considered to be the plot's canopy volume.
- Canopy Cover: Canopy cover can be estimated from LiDAR data as the ratio of above-ground points (or, canopy points) to the total number of LiDAR points in a given area. First, a grid with user-defined cell dimensions was assigned to each plot and then, for each cell in the grid, the LiDAR points are split into two groups – canopy points and bare earth points – using a user-defined threshold that is applied to the height of a point above the bare earth in order to decide its classification. The ratio of number of canopy points to the total number of LiDAR points in each cell is considered as the canopy cover for that cell. The average of the canopy cover estimated for all the cells within each plot is assigned as the canopy cover for that plot.
- Height Histogram: To capture more information of the distribution of the LiDAR points in each plot, the height histogram of each plot is calculated, which can be considered as the input features in the predictive models. This allows to delineate plant genotypes that portray different plant growth patterns.
- Hyperspectral Vegetation Indices: From the obtained hyperspectral images from the calibrated system, the average spectra values of the plots are calculated after masking the shadow and soil pixels. The average spectra values are used to extract the 36 hyperspectral vegetation indices listed in Liang et al. [18].

Finally, the above features extracted from LiDAR and hyperspectral data are used in Support Vector Regression (SVR) models to predict the end-of-season biomass.

EXPERIMENTAL RESULTS

Simultaneous LiDAR-Camera Calibration

In order to conduct a feature-based simultaneous LiDAR-camera calibration, the UAV is flown over a calibration field, as shown in Figure 2, that consists of sixteen horizontally placed highly reflective sign boards (B0-B15), five hut-shaped targets with the two faces used as planar features (PV0-PV9) and its ridges used as linear features (LH0-LH4), two building facades (PV10-PV11), and one building roof (PV12). The corners of highly reflective sign boards are distinctly identifiable in RGB images and are hence, used as point-to-point pairings between images and point-to-plane pairings between images and LiDAR. Moreover, the hut ridges are also measure in imagery in order for them to be used as linear feature pairings between imagery and LiDAR. All these features would ensure enough control along all the directions (i.e., X, Y, Z-directions). In this experiment, the flight path of the UAV comprises six flight lines each at 15 m and 25 m flying height and two flight lines at 45 m flying height above the ground, with different directions and lateral distance between the flight lines.
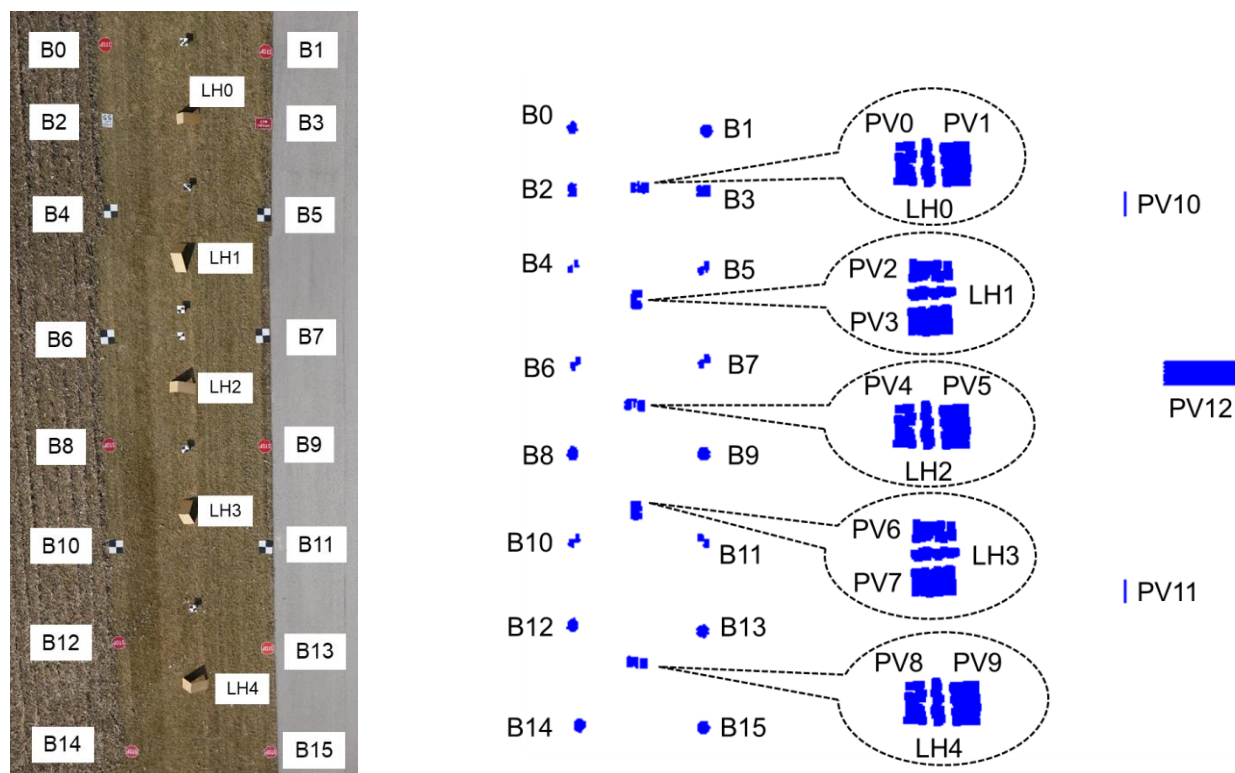
Figure 2. Calibration test field for simultaneous LiDAR-camera calibration.

The qualitative evaluation of the calibration results is done by showing the alignment in object space by computing the 3D mapping frame coordinates for all the LiDAR and image points, as shown in Figure 3. Figure 3 indicates that the corners of the highly reflective sign boards and checkerboard targets measured in different images align well with the high intensity LiDAR points. Similarly, the image points along the hut ridge are aligned in 3D with the corresponding LiDAR points.
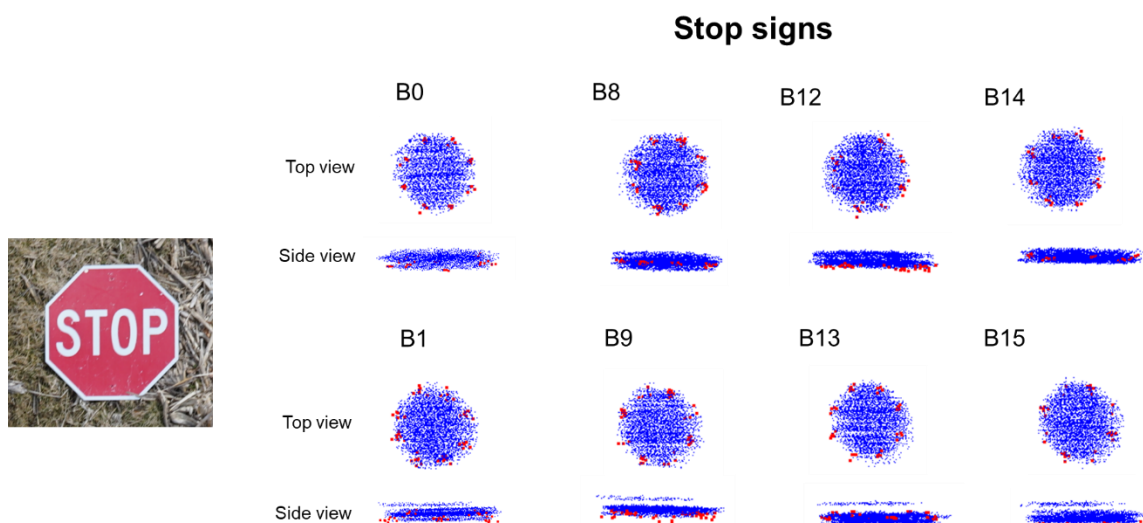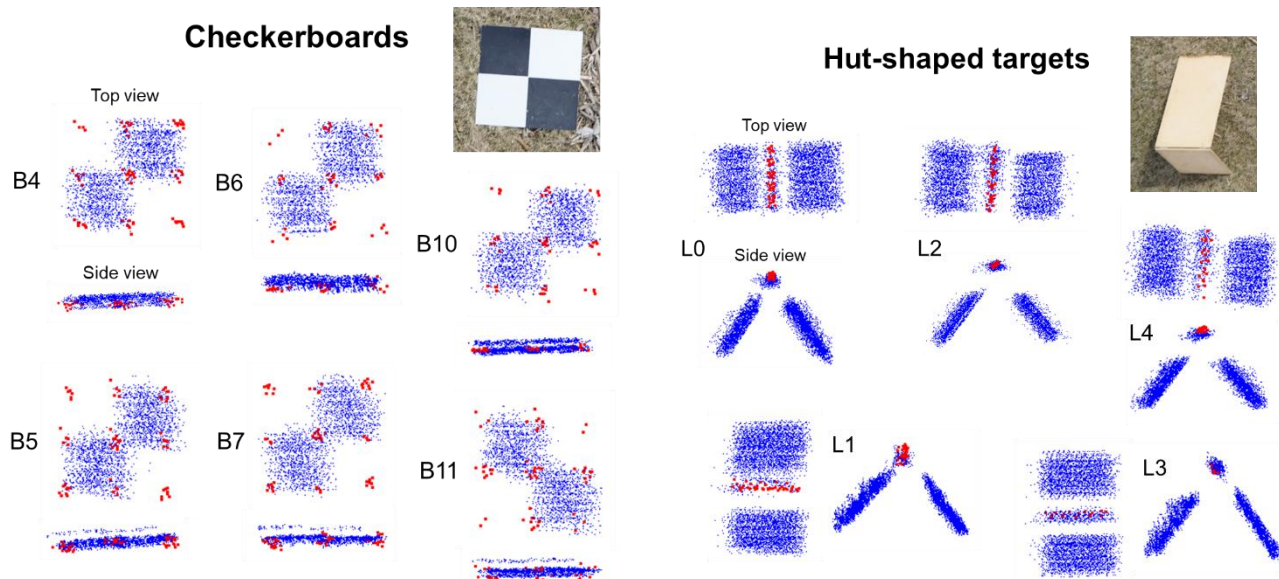
Figure 3. Qualitative evaluation of 3D alignment between LiDAR (blue) and image points (red) after calibration for the highly reflective stop signs, checkerboards, and hut-shaped targets captured by the UAV.

The initial approximations of all the mounting parameters and the final results (along with their standard deviations) after calibration are listed in Table 1. The square root of the a-posteriori variance factor $(\hat{\sigma}_o)$ representing the average compatibility between all the conjugate and pseudo-conjugate point pairings is 3 cm after calibration in this case. This is better than the expected accuracy of around 5-6 cm for an average flying height of 20 m according to the accuracies of the hardware involved. The RMSE of normal distance of LiDAR and image points from best-fitting plane/line for extracted features after calibration were found to lie in the range of 2.5 to 4.5 cm. The RGB orthophoto generated using the images captured by the onboard RGB camera at 25 m flying height and using the estimated camera mounting parameters is shown in Figure 4.

Table 1. Mounting parameters before and after calibration of the UAV-based system.

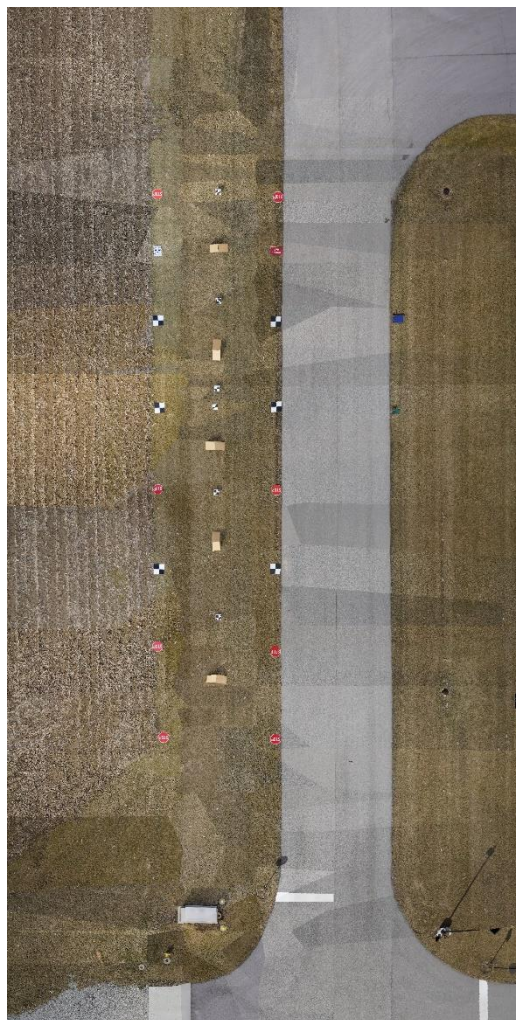| VLP-16 LiDAR Unit Mounting Parameters $\left(r_{Lu'}^b\right)\left(R_{Lu'}^b\right)$						
	ΔX (m)	ΔY (m)	ΔZ (m)	$\Delta\omega$ (°)	$\Delta\phi$ (°)	$\Delta\kappa$ (°)
Initial	-0.10	-0.03	0	0	0	0
Final	-0.1071	-0.0301	0	0.7813	-0.1728	0.3065
Std. Dev.	0.0180	0.0117	Fixed	0.0166	0.0334	0.0432
Sony α7R-III Camera Mounting Parameters $\left(r_C^b\right)\left(R_C^b\right)$						
	ΔX (m)	ΔY (m)	ΔZ (m)	$\Delta\omega$ (°)	$\Delta\phi$ (°)	$\Delta\kappa$ (°)
Initial	0.13	-0.03	0.02	180	0	-90
Final	0.1379	0.0174	0.0820	180.5570	0.8639	-90.0883
Std. Dev.	0.0573	0.0579	0.0964	0.0996	0.1009	0.0902

Figure 4. RGB orthophoto generated using images captured at 25 m flying height and the camera mounting parameters estimated after calibration.

Hyperspectral Push-broom Scanner Calibration

For this study, twelve targets are used as tie features for boresight calibration of hyperspectral push-broom scanner. The ground coordinates of all the checkerboard targets were surveyed by a Topcon GR-5 GNSS receiver. The targets are identified in the original hyperspectral scenes and the image point coordinates are measured using Envi 4.5.4 software. The estimated boresight angles for were: $\omega = 0.3440°, \phi = -0.9490°, \kappa = -0.1160°$. The accuracy of the estimated boresight angles is qualitatively checked by visually inspecting the ortho-rectified mosaics using the estimated boresight angles using the proposed calibration strategy. The ortho-rectified mosaics are generated by the SpectralView software from Headwall. Figure 5 shows the ortho-rectified mosaic generated using the images captured at 25 m flying height.
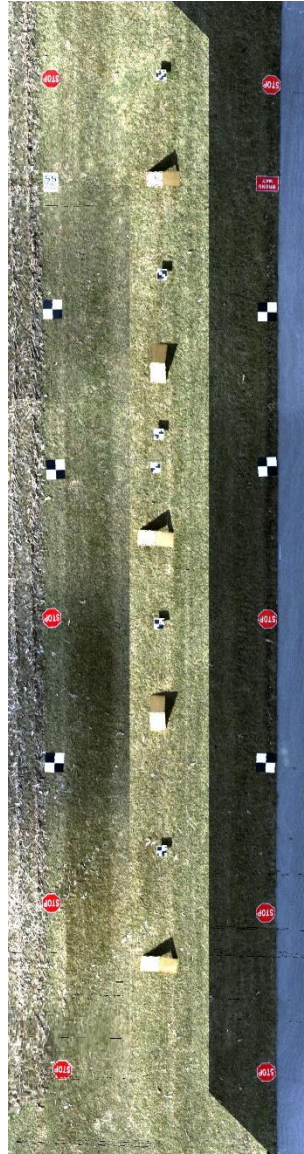
Figure 5. Hyperspectral orthomosaic generated using images captured at 25 m flying height and the boresight parameters estimated after calibration.

Derived ground coordinates of the targets from the boresight calibration are compared with the surveyed coordinates of the targets for a quantitative assessment of the proposed calibration strategy. The RMSE of the differences along the XYZ directions were observed to be (0.032 m, 0.015 m, 0.095 m), respectively. The RMSE in the vertical direction is significantly worse than the planimetric RMSE. The relatively worse vertical accuracy as represented by the RMSE is hypothesized to be caused by the intersection geometry for conjugate light rays. However, the planimetric RMSE is less than the spatial resolution of 4 cm provided by the hyperspectral push-broom scanner.

Biomass Prediction using Geometric and Spectral Characteristics of Crops

The UAV-based mobile mapping system is flown over an agricultural field comprising different plots consisting of plants with different genotypes of the sorghum, henceforth denoted as hybrid calibration panel. The forthcoming results are generated for the hybrid calibration panel in order to predict the biomass for the different genotypes.

The Digital Terrain Model (DTM) of the fields contains the bare earth height information required for estimation of canopy height from the LiDAR point clouds, which is derived using the LiDAR data acquired before emergence of the plants and is assumed to be constant throughout the growing season. Then, the Digital Surface Model (DSM) is generated by subtracting the height of bare earth from the height of each point in the LiDAR data acquired during the season. Figure 6. shows the DSM obtained for the hybrid calibration panel for multiple dates in the 2017 growing season.

| 2017/06/27 | 2017/07/07 | 2017/07/25 | 2017/08/23 |
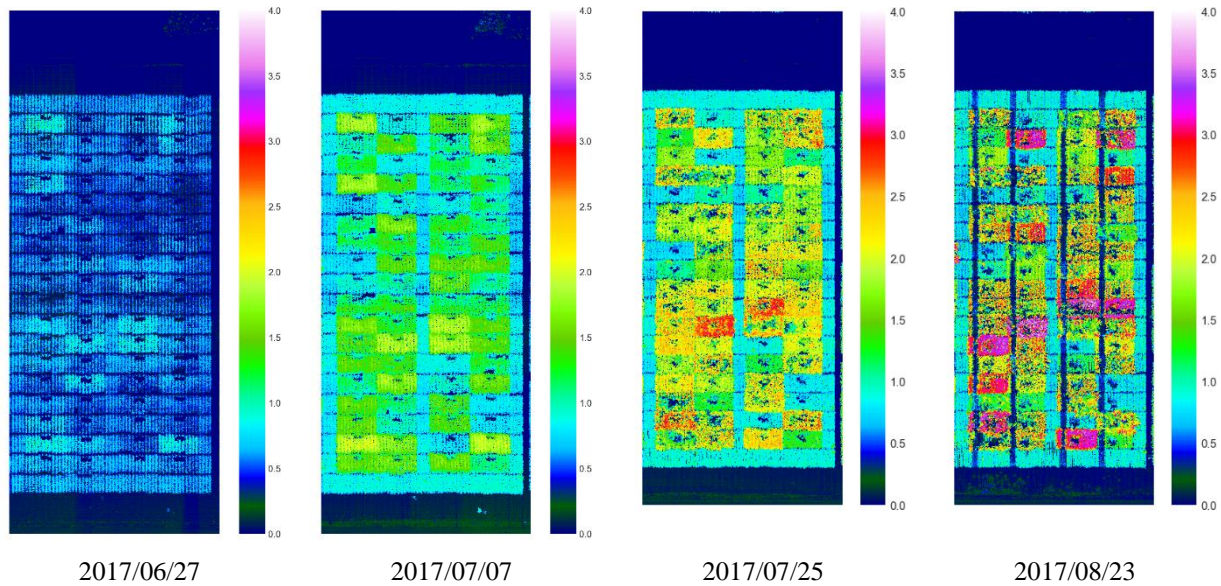
Figure 6. DSM of multiple dates for the hybrid calibration panel in the 2017 growing season.

From the LiDAR point cloud of each date, the 30th, 50th, 75th, 90th, 95th, 99th, and 100th percentile height values were extracted for each plot. Figure 7 shows the 90th percentile height extracted for the hybrid calibration panel in the 2017 growing season.
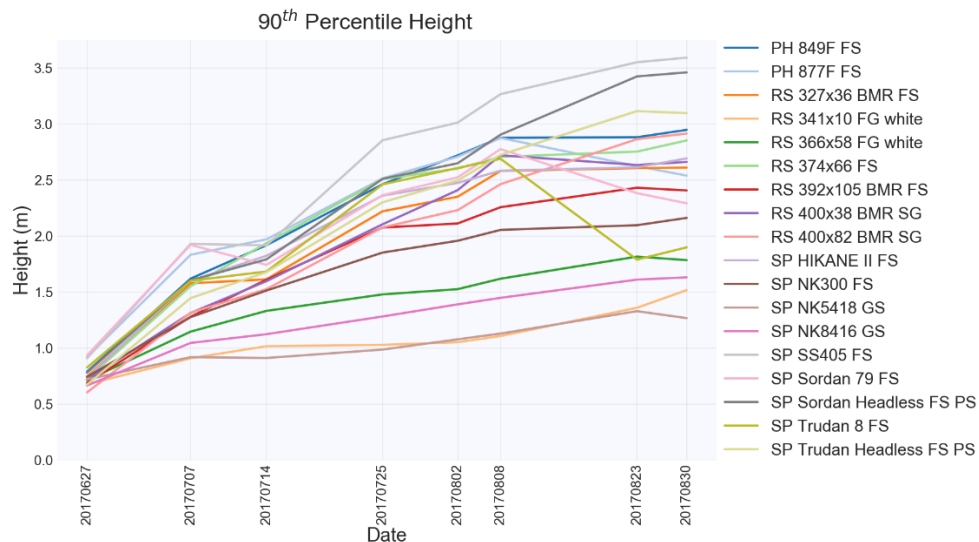

Figure 7. 90th height for the hybrid calibration panel varieties in the 2017 growing season.

The LiDAR-based 3D point cloud was used to estimate the canopy cover using a cell size of 8×8 cm. The 10th, 20th, 30th, 40th, 50th, and 75th percentile of the maximum height of each plot were considered as the threshold values to classify the points as canopy points or bare earth points. Figure 8 shows the estimated canopy cover for one of the varieties using 40th percentile of maximum height as the threshold in the hybrid calibration panel in the 2018 growing season.
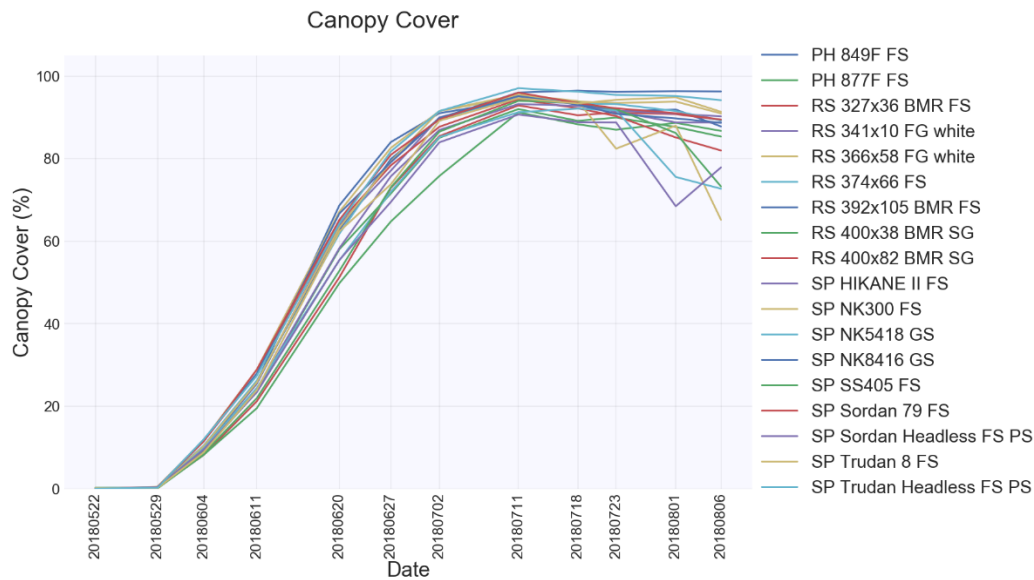

Figure 8. Canopy Cover estimated for the hybrid calibration panel in the 2018 growing season.

To capture more information of the distribution of the LiDAR points in each plot, the height histogram of each plot is calculated (using 25 equally spaced bins in this study), which can further be considered as input features in biomass predictive models. Figure 9 shows the histograms for two varieties with different plant growth patterns in the hybrid calibration panel during the 2017 growing season.
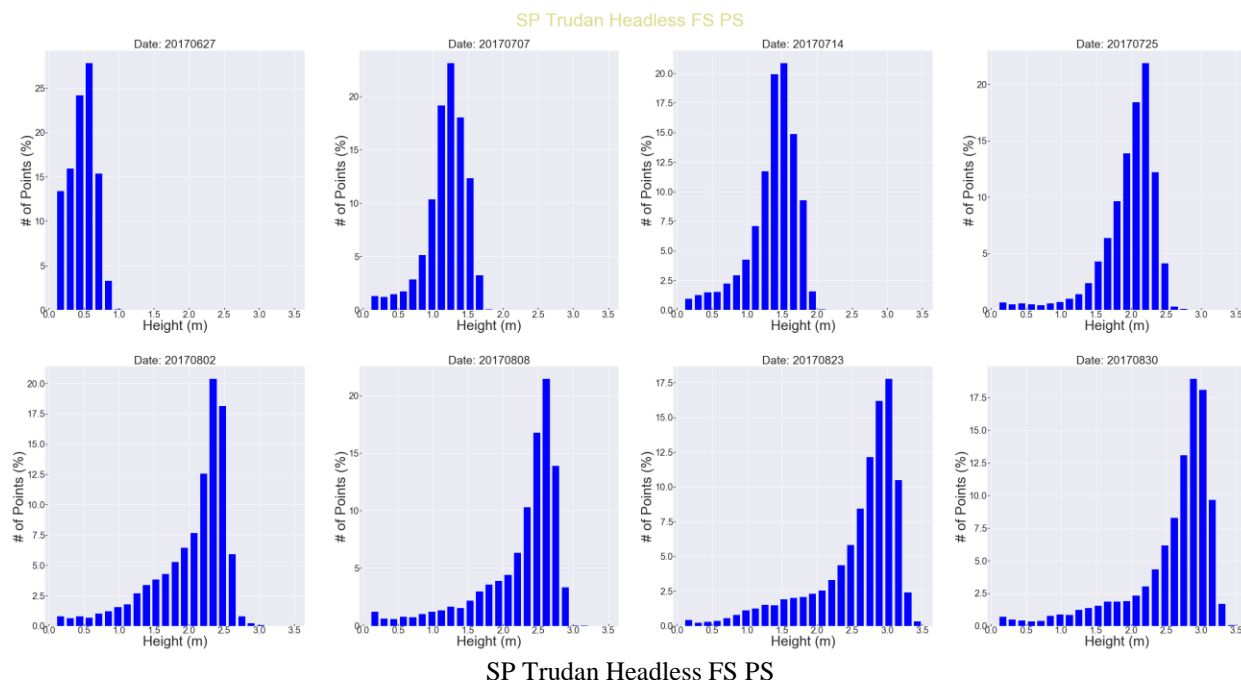

SP Sordan 79 FS
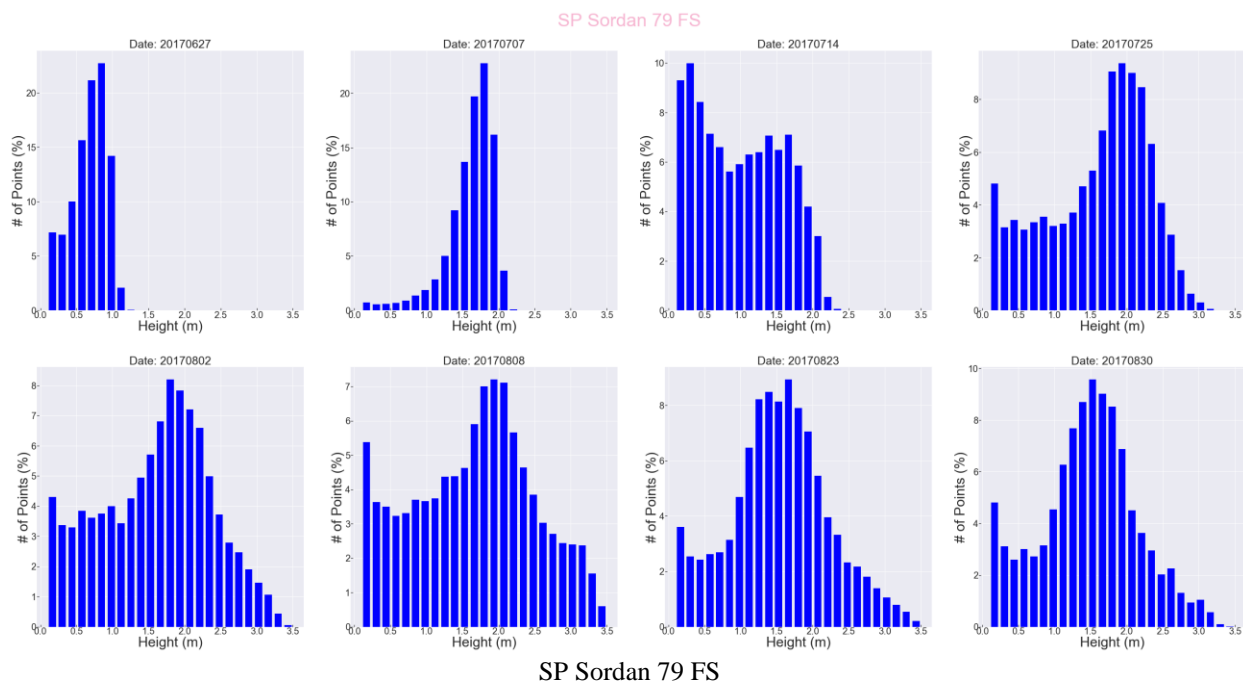
Figure 9. Height histogram for two varieties in the hybrid calibration panel across the 2017 growing season.

From the hyperspectral data, the average spectral values were calculated for each plot in the hybrid calibration panel after masking the shadow and soil pixels. Figure 10 shows the average spectra of 18 varieties of sorghum in the hybrid calibration panel on July 25th, 2017. Figure 11 shows the average spectra of one variety of sorghum in the hybrid calibration panel during the 2017 growing season.
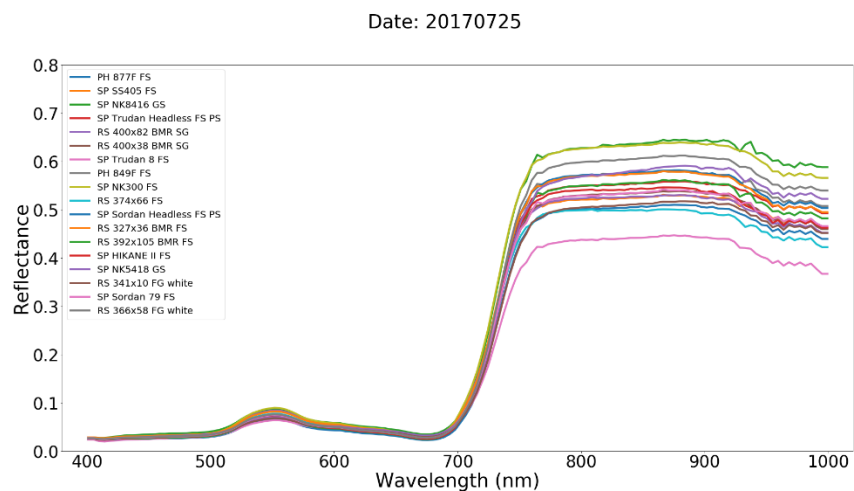

Figure 10. Average spectra of 18 varieties of sorghum in the hybrid calibration panel on July 25th, 2017.
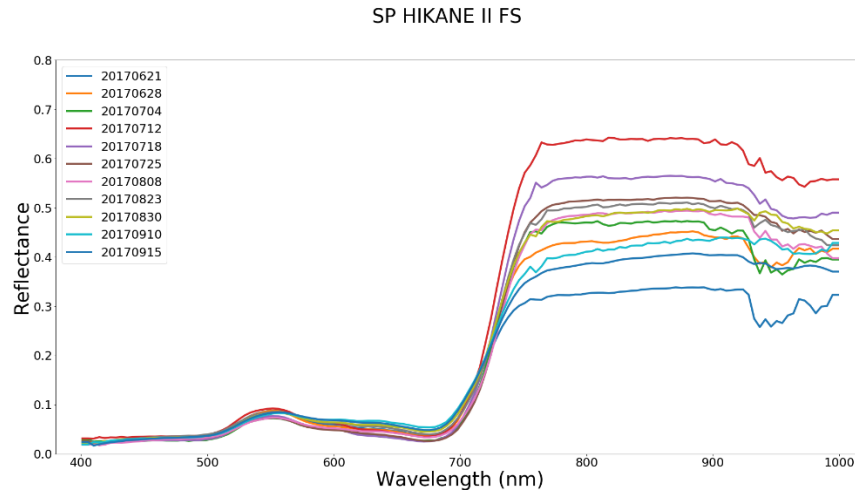
SP HIKANE II FS

Figure 11. Average spectra of one variety of sorghum in the hybrid calibration panel during the 2017 growing season.

From the average spectra, 36 hyperspectral vegetation indices were extracted and used in Support Vector Regression (SVR) models to predict end of season biomass. The parameter setting for SVR is described in our previous work by Zhang et al. [19]. The ground reference biomass was measured at the end of the growing season. Figure 12 shows the accuracy of end-of-season biomass predictions as compared to the ground truth for biomass in the 2017 growing season using indices extracted from hyperspectral data as well as LiDAR features of each date individually and in combination with the earlier dates. The accuracy of prediction is denoted by the R^2 value representing the quality of fit of a straight line to the predicted versus the ground truth biomass of the plants. It can be seen that the biomass prediction using both LiDAR-based and hyperspectral features together provides the most accurate results as compared to the predictions using features from each of these modalities separately. Moreover, such a non-destructive biomass prediction model would facilitate the estimation of end-of-season biomass in the middle of the growing season, subject to sufficient plant traits captured by these sensors.
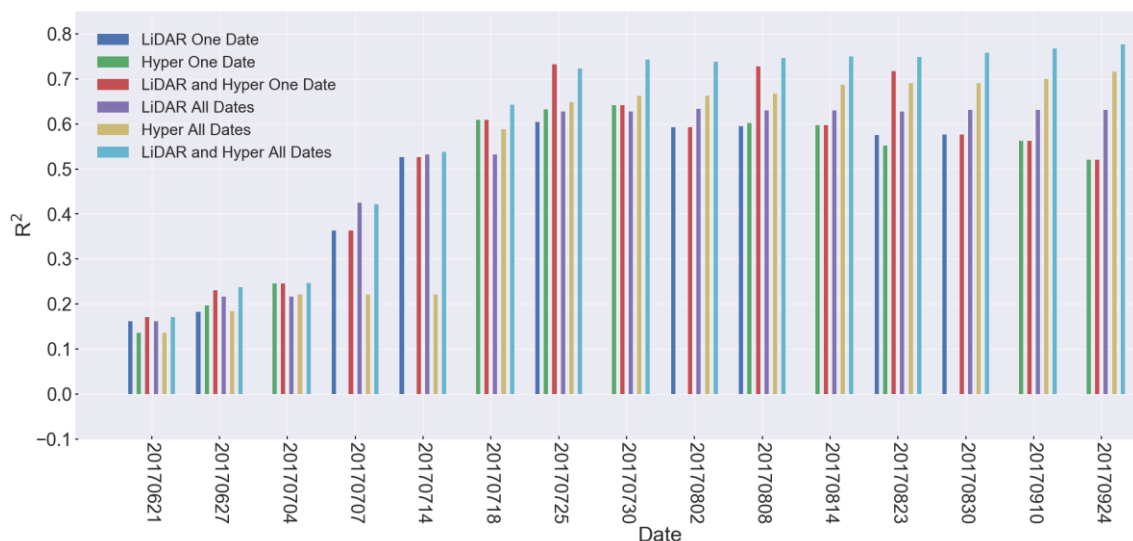

Figure 12. The R^2 for end-of-season predictions using hyperspectral and LiDAR data collected on different dates during the 2107 growing season.

CONCLUSIONS AND RECOMMENDATIONS FOR FUTURE WORK

In this paper, we introduced a UAV-based multi-sensor platform for high throughput phenotyping. The UAV platform was mounted with a LiDAR unit, an RGB camera, and a hyperspectral push-broom scanner and we proposed a calibration strategy in order to derive accurately georeferenced products from each of these sensors. The simultaneous LiDAR-camera calibration strategy as well as the strategy for hyperspectral push-broom scanner were both observed to attain an accuracy of upto 3 cm, which is better than the expected accuracy of the data acquired by the system, keeping in mind the accuracy specifications of the hardware involved. Finally, the calibrated data from the different sensors were used to extract plant characteristics that aided in developing a model for non-destructive biomass prediction for different genotypes of a crop (here, sorghum). Such a non-destructive biomass prediction model would facilitate the estimation of end-of-season biomass in the middle of the growing season, subject to sufficient plant traits captured by these sensors.

REFERENCES

[1] Tilman, D., Balzer, C., Hill, J., & Befort, B. L. (2011). Global food demand and the sustainable intensification of agriculture. Proceedings of the National Academy of Sciences, 108(50), 20260-20264.

[2] Phillips, R. L. (2010). Mobilizing science to break yield barriers. Crop Science, 50(Supplement_1), S-99.

[3] Araus, J. L., & Cairns, J. E. (2014). Field high-throughput phenotyping: the new crop breeding frontier. Trends in plant science, 19(1), 52-61.

[4] Habib, A., Kersting, A. P., Shaker, A., & Yan, W. Y. (2011). Geometric calibration and radiometric correction of LiDAR data and their impact on the quality of derived products. Sensors, 11(9), 9069-9097.

[5] Atanacio-Jiménez, G., González-Barbosa, J. J., Hurtado-Ramos, J. B., Ornelas-Rodríguez, F. J., Jiménez-Hernández, H., García-Ramirez, T., & González-Barbosa, R. (2011). Lidar velodyne hdl-64e calibration using pattern planes. International Journal of Advanced Robotic Systems, 8(5), 59.

[6] Glennie, C., Brooks, B., Ericksen, T., Hauser, D., Hudnut, K., Foster, J., & Avery, J. (2013). Compact multipurpose mobile laser scanning system—Initial tests and results. Remote Sensing, 5(2), 521-538.

[7] Ravi, R., Shamseldin, T., Elbahnasawy, M., Lin, Y. J., & Habib, A. (2018). Bias Impact Analysis and Calibration of UAV-Based Mobile LiDAR System with Spinning Multi-Beam Laser Scanner. Applied Sciences, 8(2), 297.

[8] Habib, A., Morgan, M., & Lee, Y. R. (2002). Bundle adjustment with self–calibration using straight lines. The Photogrammetric Record, 17(100), 635-650.He, Mengwen, et al. "Pairwise LIDAR calibration using multi-type 3D geometric features in natural scene." Intelligent Robots and Systems (IROS), 2013 IEEE/RSJ International Conference on. IEEE, 2013.

[9] Furukawa, Y., & Ponce, J. (2009). Accurate camera calibration from multi-view stereo and bundle adjustment. International Journal of Computer Vision, 84(3), 257-268.

[10] Delara, R., Mitishita, E. A., & Habib, A. (2004, July). Bundle adjustment of images from non-metric CCD camera using LIDAR data as control points. In International Archives of XXth ISPRS Congress (pp. 13-19).

[11] Castorena, J., Kamilov, U. S., & Boufounos, P. T. (2016, March). Autocalibration of LIDAR and optical cameras via edge alignment. In Acoustics, Speech and Signal Processing (ICASSP), 2016 IEEE International Conference on (pp. 2862-2866). IEEE.

[12] Levinson, J., & Thrun, S. (2013, June). Automatic Online Calibration of Cameras and Lasers. In Robotics: Science and Systems (pp. 24-28).

[13] R. Muller, M. Lehner, R. Muller, P. Reinartz, M. Schroeder, and B. Vollmer, "A program for direct georeferencing of airborne and spaceborne line scanner images," International Archives of Photogrammetry Remote Sensing and Spatial Information Sciences, vol. 34, no. 1, pp. 148–153, 2002.

[14] C.-K. Yeh and V. J. Tsai, "Direct georeferencing of airborne pushbroom images," Journal of the Chinese Institute of Engineers, vol. 38, no. 5, pp. 653–664, 2015.

[15] A. Zhang, S. Hu, X. Meng, L. Yang, and H. Li, "Toward High Altitude Airship Ground-Based Boresight Calibration of Hyperspectral Pushbroom Imaging Sensors," Remote Sensing, vol. 7, no. 12, pp. 17297–17311, 2015.

[16] Ravi, R., Lin, Y. J., Elbahnasawy, M., Shamseldin, T., & Habib, A. (2018). Simultaneous System Calibration of a Multi-LiDAR Multicamera Mobile Mapping Platform. IEEE Journal of selected topics in applied earth observations and remote sensing, 11(5), 1694-1714.

[17] Habib, A., Zhou, T., Masjedi, A., Zhang, Z., Flatt, J. E., & Crawford, M. (2018). Boresight Calibration of GNSS/INS-Assisted Push-Broom Hyperspectral Scanners on UAV Platforms. IEEE Journal of Selected Topics in Applied Earth Observations and Remote Sensing, 11(5), 1734-1749.

[18] Liang, L., Di, L., Zhang, L., Deng, M., Qin, Z., Zhao, S., & Lin, H. (2015). Estimation of crop LAI using hyperspectral vegetation indices and a hybrid inversion method. Remote Sensing of Environment, 165, 123-134.

[19] Zhang, Z., Masjedi, A., Zhao, J., & Crawford, M. M. (2017, July). Prediction of Sorghum biomass based on image based features derived from time series of UAV images. In 2017 IEEE International Geoscience and Remote Sensing Symposium (IGARSS) (pp. 6154-6157). IEEE.